

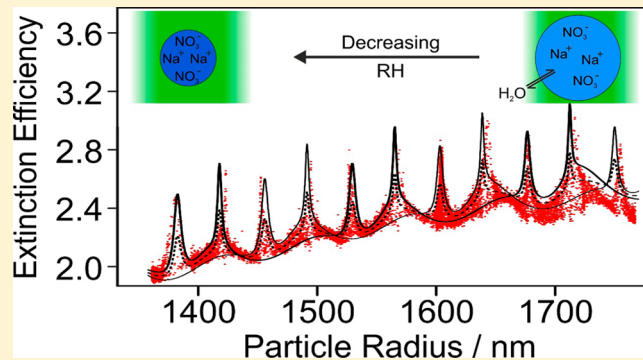
# Direct Measurements of the Optical Cross Sections and Refractive Indices of Individual Volatile and Hygroscopic Aerosol Particles

B. J. Mason,<sup>†</sup> M. I. Cotterell,<sup>†</sup> T. C. Preston,<sup>‡</sup> A. J. Orr-Ewing,<sup>†</sup> and J. P. Reid\*,<sup>†</sup>

<sup>†</sup>School of Chemistry, University of Bristol, Bristol, BS8 1TS, U.K.

<sup>‡</sup>Department of Atmospheric and Oceanic Sciences and Department of Chemistry, McGill University, 801 Sherbrooke West, Montreal, QC, Canada H3A 0B9

**ABSTRACT:** We present measurements of the evolving extinction cross sections of individual aerosol particles (spanning 700–2500 nm in radius) during the evaporation of volatile components or hygroscopic growth using a combination of a single particle trap formed from a Bessel light beam and cavity ring-down spectroscopy. For single component organic aerosol droplets of 1,2,6-hexanetriol, polyethylene glycol 400, and glycerol, the slow evaporation of the organic component (over time scales of 1000 to 10 000 s) leads to a time-varying size and extinction cross section that can be used to estimate the refractive index of the droplet. Measurements on binary aqueous–inorganic aerosol droplets containing one of the inorganic solutes ammonium bisulfate, ammonium sulfate, sodium nitrate, or sodium chloride (over time scales of 1000 to 15 000 s) under conditions of changing relative humidity show that extinction cross-section measurements are consistent with expectations from accepted models for the variation in droplet refractive index with hygroscopic growth. In addition, we use these systems to establish an experimental protocol for future single particle extinction measurements. The advantages of mapping out the evolving light extinction cross-section of an individual particle over extended time frames accompanied by hygroscopic cycling or component evaporation are discussed.



## I. INTRODUCTION

One of the largest uncertainties in quantifying the anthropogenic forcing on climate is the magnitude of the direct effect, the scattering and absorption of both solar and terrestrial light by aerosol particles.<sup>1–4</sup> The flux of light scattered and absorbed by a single homogeneous spherical particle is determined by the extinction cross-section,  $\sigma_{\text{ext}}$ , which is dependent on the complex refractive index (RI) and radius of the particle. Further, the radii of aerosol particles are affected by their hygroscopicity, the equilibrium capacity of a particle to absorb water and grow in size as the relative humidity (RH) surrounding the particle increases. Not only does hygroscopicity determine the growth in geometric size, but the changing concentrations of solutes within the particle lead to a varying RI with RH and particle size. Other than dispersed mineral dust, there are only a small number of atmospherically relevant inorganic species, predominantly ammonium sulfate, ammonium bisulfate, sodium chloride, sodium nitrate, and ammonium nitrate.<sup>1–4</sup> These inorganic salts make up a significant proportion of the mass of atmospheric aerosol.<sup>4,5</sup> In contrast, the diversity of atmospheric organic components and chemical functionalities in both gaseous and aerosol phases is considerable. Improved characterisations of the dependency of the RI of particles on RH are critical to refine the models

that are used to describe light scattering by homogeneous particles at ambient RHs.

Cavity ring-down spectroscopy (CRDS) is a well-established technique that is used to determine extinction properties of both ambient and laboratory generated aerosol.<sup>6–9</sup> In the laboratory, a typical aerosol CRDS measurement involves passing an aerosol ensemble, with a known size distribution, composition, and number density, through an optical cavity. A reduction in the cavity ring-down time (RDT),  $\tau$ , from that of the empty cavity value,  $\tau_0$ , is used to determine the effective extinction cross-section,  $\sigma_{\text{ext}}$ .<sup>9–12</sup> Comparisons with Mie theory can be made to determine the aerosol RI when measurements of  $\sigma_{\text{ext}}$  are performed at a number of particle sizes. This technique has been used for studies of coated aerosols,<sup>11</sup> absorbing aerosols at high RH<sup>13</sup> and internally mixed organic/inorganic aerosols.<sup>14</sup> However, the sources of error and uncertainty for ensemble CRDS measurements can be varied and considerable in magnitude.<sup>8</sup> In particular, the size range of the size-selected aerosol ensemble and the number concentration in the optical cavity for any one measurement must both be well-defined for an accurate determination of  $\sigma_{\text{ext}}$ .<sup>9</sup> CRDS

**Received:** January 15, 2015

**Revised:** May 18, 2015

**Published:** May 19, 2015

measurements on a single aerosol particle, in which the particle radius can be measured and the particle can be studied over an extended period of time, could provide clear advantages over ensemble measurements.

The first single particle CRDS measurements were reported by Butler et al. and were accompanied by a partner paper by Miller and Orr-Ewing which outlined the expected influence of the cavity standing wave on the shape of the measured ring-down decay and the value of the determined RDT.<sup>15,16</sup> In the paper by Butler et al., a quasi-monodisperse aerosol ensemble of polystyrene beads was present in a closed CRDS instrument. The measurements were made sufficiently quickly ( $\sim 1$  kHz) that transits of single particles across the CRDS beam could be observed. Walker et al. developed a single aerosol CRDS technique that introduced an optical trap formed by a Bessel laser beam (BB), a complex optical interference pattern consisting of a bright central core surrounded by multiple rings.<sup>17</sup> This innovation allowed controlled measurements to be made on a single particle trapped over an indefinite period of time. When the directionality of the optical force along the BB propagation direction is countered by a gas flow, single micrometer-sized aerosol can be confined and spatially manipulated over macroscopic (millimeter) distances with micrometer-resolution.<sup>18,19</sup> The combination of a BB trap with CRDS enables accurate single particle  $\sigma_{\text{ext}}$  measurements to be made for a multitude of well-defined particle compositions through rigorous laboratory studies.

The extinction cross-section of a single particle trapped in the center of the ring down beam can be determined from measured ring-down times recorded without and with a particle ( $\tau_0$  and  $\tau$  respectively):<sup>16</sup>

$$\frac{1}{\tau} - \frac{1}{\tau_0} = \frac{2c\sigma_{\text{ext}}}{\pi L w_0^2} \quad (1)$$

In eq 1,  $c$  is the speed of light,  $L$  is the cavity length and  $w_0$  is the beam waist at the cavity center. The extinction efficiency,  $Q_{\text{ext}}$ , of the particle can then be calculated providing that the geometric cross-section,  $\sigma_{\text{geo}}$ , is known:

$$Q_{\text{ext}} = \frac{\sigma_{\text{ext}}}{\sigma_{\text{geo}}} \quad (2)$$

For a spherical particle,  $\sigma_{\text{geo}}$  can be determined from the particle radius,  $r$ . Using the theory developed in ref 15, Mason et al. recently reported experiments that demonstrated the adjustment that must be made to the Mie simulations of  $Q_{\text{ext}}$  because of the movement of a trapped particle within the standing wave of the optical cavity.<sup>20</sup> Typically, particles with radii  $< 2 \mu\text{m}$  were trapped within a  $5-7 \mu\text{m}$  BB core, in which the particle was free to move through Brownian motion traversing several nodes and antinodes of the CRDS standing wave ( $\lambda = 532 \text{ nm}$ ). For a single particle of a given radius and RI, a spread in  $Q_{\text{ext}}$  values is then observed and is attributed to the particle motion.<sup>20</sup> Cavity standing wave (CSW) Mie simulations can be performed for the limiting cases where the particle is positioned at a node or antinode, with these two scenarios representing the extremes in the values of  $Q_{\text{ext}}$  defining an envelope within which all the measured  $Q_{\text{ext}}$  data points should be contained (in the absence of other sources of experimental noise).<sup>15</sup>

In the first section of this paper, we establish the scope and limitations of the single particle CRDS technique. Model single-component organic aerosol samples are used to determine the

reproducibility of RI measurements under ideal conditions, the effect of the RDT fluctuations on the precision of the retrieved RI, and the range of rates of size change over which accurate optical extinction measurements can be made. The second section examines the hygroscopic response in  $Q_{\text{ext}}$  of several different aqueous inorganic particles, specifically ammonium bisulfate (AB), sodium nitrate (SN), ammonium sulfate (AS), and sodium chloride (SC). The relationships between RI/concentration and concentration/water-activity of these atmospherically relevant salts have previously been parametrized by Tang and co-workers.<sup>21-24</sup> We use these parametrizations to describe the RI variation with droplet radius for our experiments, relying on accurate RH probe measurements.<sup>9,14,19,25-28</sup> Our objective is to validate and benchmark the single particle CRDS technique by providing comprehensive measurements of the optical properties of systems that have been well-characterized previously.

## II. EXPERIMENTAL DESCRIPTION

A continuous wave, single mode laser beam (Coherent Verdi,  $\lambda = 532 \text{ nm}$ ) was directed through a polarization beam splitter cube and the transmitted light passed through a conically shaped lens, an axicon (Altechna, apex angle =  $178^\circ$ ), to generate a Bessel beam (BB). A beam expander was used to reduce the core size of the BB by a factor of approximately 10 (magnification,  $M \approx 0.1$ ). This beam was then directed into a trapping cell, propagating in a vertical direction,  $y$  coordinate, counter to a downward directed gas flow to form a "Bessel-beam/gas-flow" trap. For the measurements described here, the core radius was measured as  $3.6 \mu\text{m}$  in the trapping region, the propagation distance ( $z_{\text{max}}$ ) measured as  $6.75 \text{ mm}$  and the semiapex angle was calculated to be  $7.04^\circ$ . The total laser power of the BB before the trapping cell was typically between 380 and 760 mW and the number of rings in the trapping volume was measured to be between 30 and 37. The power of the trapping core can be estimated by dividing the laser power by the number of rings yielding a laser power range of 10–26 mW.

The reflected light from the polarization beam splitter cube was directed toward an acousto-optic deflector which diffracted the beam into a series of spots. The first-order spot was selected and coupled into an optical cavity consisting of two highly reflective mirrors (Layertec) with reflectivities greater than 99.98%, separated by a distance of 0.5 m. One of the mirrors was mounted on a piezo ring actuator (Piezomechanik) which allowed the cavity length to be modulated by an amplitude of  $\sim 2 \mu\text{m}$  at a rate of  $\sim 20 \text{ Hz}$ . When the cavity length was equal to an integer number of wavelengths of the injected beam ( $\lambda = 532 \text{ nm}$ ), buildup of light occurred, and a standing wave formed (along the  $z$  coordinate). Small  $\sim 2 \text{ mm}$  holes in the trapping cell windows allowed the TEM<sub>00</sub> mode of the cavity ring-down beam to bisect the BB in the trapping cell. The light exiting the optical cavity was continuously monitored by a photodiode (RedWave Laboratories, D101). When the buildup of light detected reached a threshold intensity, a TTL pulse was sent to the acousto-optic deflector, deflecting the beam from the optical cavity and leading to a ring down of the light within the cavity. The background RDT,  $\tau_0$ , of the optical cavity was typically  $22 \pm 0.2 \mu\text{s}$  and was measured at a rate of 2–10 Hz. Here, the uncertainty in the  $\tau_0$  signal is defined as 1 standard deviation of at least 100 s of data.

For each extinction measurement set, an aqueous solution of an inorganic salt or organic component ( $50-120 \text{ g L}^{-1}$ ) was

nebulized using a medical nebulizer (Omron) and the aerosol plume passed into the trapping cell until a single particle was confined within the BB/gas-flow trap. The gas flow for the measurements described here was typically 100 SCCM, consisting of a mixture of dry and humidified nitrogen gas, the RH of which could be controlled. The RH within the trapping cell was continuously measured using a Honeywell capacitance probe (HIH-4602C). A camera (Thorlabs, DCC1545M) coupled to a long working distance objective (MOTIC,  $\times 20$ , NA = 0.42) was used to capture the elastic light scattering over a fixed angular range (phase function) between  $65^\circ$  and  $112^\circ$  with respect to the BB propagation direction. These phase functions (PFs) were acquired at a rate of 1 Hz, from which the radius of the particle was determined by comparison with Mie theory simulations. In addition to monitoring PFs, this camera was spatially calibrated (1 pixel =  $0.9\ \mu\text{m}$ ) and used to monitor the vertical ( $y$ ) coordinate of the particle.

Both the trapping cell and the final mirror that steered the BB vertically into this cell were mounted on a micrometre translation stage. The position of a trapped particle was optimized in all transverse directions to the CRD beam to place it at the beam center, giving a minimum in the observed cavity RDT. This optimization was performed by varying the BB's transverse horizontal position ( $x$  coordinate) by adjusting the micrometre translation stage, as well as by varying the laser power in the BB to control the vertical position ( $y$  coordinate). Using the equations given by Walker et al., our calculations of the dependence of the measured RDT on the transverse position of the particle within our TEM<sub>00</sub> CRD beam (of beam waist  $\sim 271\ \mu\text{m}$ ) show that  $\tau$  is relatively insensitive to small excursions ( $\pm 20\ \mu\text{m}$ ) in particle position from the CRD beam center.<sup>17</sup> However, large excursions in position ( $\pm 100\ \mu\text{m}$ ) can lead to significant changes. Thus, it was important to ensure that a particle was held at the center of the CRD beam. However, as the trapped particle changed size either by evaporation or hygroscopic response, the radiation pressure efficiency and equilibrium particle position along the length of the BB also changed. To maintain the particle at a fixed position, changes in optical cross-section were compensated for by varying the BB laser power continuously to keep the particle at the center of the CRD beam. The factors that govern the change in radiation pressure efficiency, and thus particle position, with changing radius for a particle trapped in a Bessel beam have been discussed in detail by Preston et al.<sup>29</sup>

### III. SCOPE AND LIMITATIONS OF THE SINGLE PARTICLE CRDS INSTRUMENT

An assessment of the scope and limitations of the single particle CRDS system is important for determining the accuracy of optical extinction measurements with the existing instrument and in identifying the refinements required to expand its capability. Given the envelope of the measured  $\tau$ , arising from the Brownian motion of the particle across the CRD standing wave, it is problematic to assign an uncertainty to each individually measured  $Q_{\text{ext}}$ . Instead, the standard deviation of  $\tau_0$  is measured at the start and end of the measurement and interpolated to yield a percentage uncertainty that should be valid for each measured  $\tau$ . The  $\tau_0$  signal noise is affected by detector noise of the photodiode that registers the decay, the cavity alignment stability and, in the case of an open cavity, the very small numbers of ambient particles.

RI measurements of three benchmark aerosol organic systems are presented, specifically 1,2,6-hexanetriol (HT), polyethylene glycol 400 (PEG-400), and glycerol. These three systems were chosen as they have distinctly different volatilities and low hygroscopicities. In the case of the PEG-400 particles, the effect of increased  $\tau_0$  signal noise on the precision of the retrieved RI is explored. For accurate RI measurements, the BB laser feedback must respond sufficiently fast that a particle is consistently confined at the center ( $\pm 20\ \mu\text{m}$ ) of the CRD beam, and a sufficiently high number of RDTs must be collected per unit of radius change. These requirements impose a maximum radius change with time ( $dr/dt$ ) that an aerosol can undergo, which subsequently dictates an upper limit on the volatility for an organic particle or change in humidity for a hygroscopic particle. Accordingly, the evaporation of a glycerol droplet is used to demonstrate the reduction in accuracy of RI determination that results when determining the optical properties of a volatile aerosol particle.

**III.a. RI Determination and the Effect of Signal Noise on RI Precision.** This section examines the extraction of refractive indices from single-particle CRDS data, using single-component droplets (with RIs that are constant throughout the measurement) as test systems. It illustrates how noise in the measurements affects the precision that can be achieved in RI determinations. The samples used are 1,2,6-hexanetriol and polyethylene glycol 400, which are chosen because their volatilities are low enough to allow measurements over a few hours.

For particles of invariant composition with radius, the RI used in the PF fitting is chosen to take a constant value estimated from the literature,  $n_1$ . This choice provides an initial estimate of the time-dependent radius,  $r_1$ , of the particle. Comparisons of the CRD data with CSW Mie simulations start with the radii estimated from the PF, but allow the RI ( $n_{532}$ ) used in the CSW Mie calculations to vary (along with  $w_0$ ) to obtain a more accurate RI at an illumination wavelength of 532 nm. Because the radius of the droplet determined from the PF is dependent on the initial choice of RI, for every trial value of  $n_{532}$  used in the CSW Mie simulations, the radius must be scaled using the empirical relation  $n_1 r_1 = n_2 r_2$ . Here,  $r_2$  is the scaled particle radius for the trial refractive index  $n_2$ . This scaled radius is used to provide an experimental droplet size and hence  $Q_{\text{ext}}$  value which is compared with the CSW Mie envelope simulations of  $Q_{\text{ext}}$ . The comparison of the measurement and simulations is evaluated by calculating the percentage  $P_v$  of  $Q_{\text{ext}}$  data points that fall outside the envelope of CSW Mie simulations obtained using limiting cases of a particle at a node and antinode. A contour plot of  $P_v$  as a function of both  $w_0$  and RI reflects the sensitivity of the fit to these parameters and the minimum in the contour plot is determined using the method described by Mason et al.<sup>20</sup> In addition to RI and  $w_0$ , a small particle radius offset was varied, independently of RI, to account for subtle miss-assignments of angular range used in the PF radius determination. For the particles described in this section, the overall change in radius from the initial estimate obtained from the phase function analysis was typically  $< 5\ \text{nm}$ .

The time-dependent trends in the radii of four 1,2,6-hexanetriol particles are shown in Figure 1 and include the data for the HT particle described in our previous publication and identified as particle "4" (Figure 1, blue dots).<sup>20</sup> The RI used in the initial radius determination from the phase function was 1.4759 ( $n_{589}$ ,<sup>20</sup> Aldrich). The particles labeled 1, 2, and 3 have corresponding RDT data, which were analyzed and fitted to

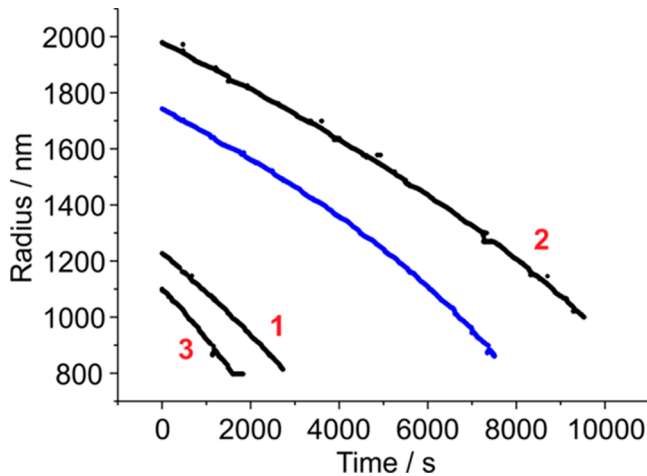


**Figure 1.** Determined radius as a function of time for four evaporating HT droplets. The initial time when PFs are recorded is denoted as  $t = 0$  s. Particles 1–3, highlighted in black, were further analyzed by CRDS. Particle 4 is the HT particle analyzed in ref 20.

CSW Mie simulations to determine the particle RI. Figure 2 shows the  $Q_{\text{ext}}$  values inferred from the measurements (red

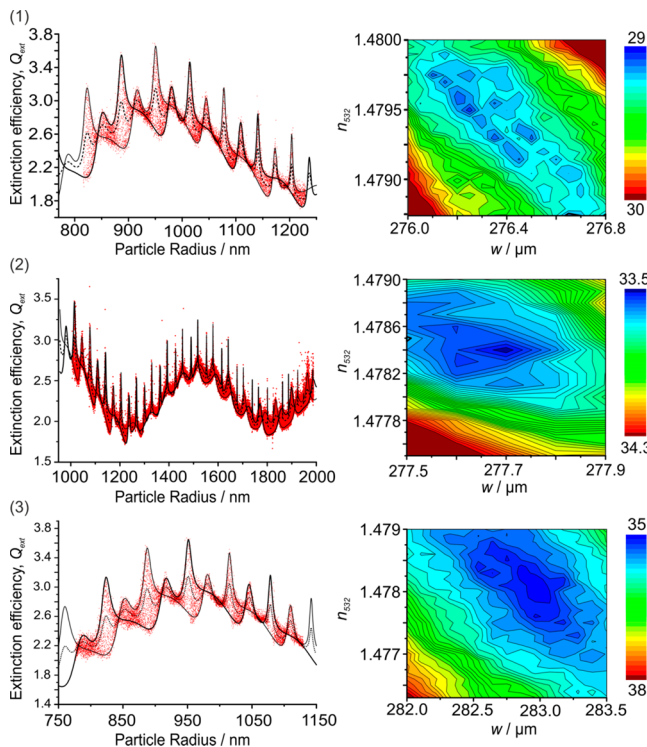


**Figure 2.** (left column) Measured  $Q_{\text{ext}}$  curves for HT particles 1, 2, and 3 (red dots) as a function of radius. CSW Mie calculations for a particle centered on a node (thin black line), an extremum (thick black line), and plane wave  $Q_{\text{ext}}$  simulation (dotted black line). (right column) Percentages of  $Q_{\text{ext}}$  points ( $P_v$ ) that lie outside the CSW Mie envelope calculated for different  $n_{532}$  and  $w_0$  trial parameters.

dots) and the best fit CSW Mie simulations (black lines) for particles 1, 2, and 3, as well as contour plots of variation of  $P_v$  with  $n_{532}$  and  $w_0$ . For each particle, the measured  $Q_{\text{ext}}$  values agree very well with the CSW Mie simulations. A best radius offset was found to be +2, +1.5, and +3 nm for particles 1–3 respectively which correspond to fractional shifts of less than

0.7% in the geometric cross-section. The  $P_v$  corresponding to minima in the contour plots, with inclusion of the corresponding radius offsets, are 28.9, 33.5, and 35.1% of points outside the CSW Mie calculation limits, for particles 1–3 respectively. For each particle, the percentage uncertainty in  $\tau_0$  was less than 1%, which manifests in Figure 2 as tight confinement of the measured  $Q_{\text{ext}}$  values within the CSW Mie simulated envelope.

At first glance, the percentages of points,  $P_v$ , lying outside the envelope defined by the CSW treatment appear to be high so it is important to consider the factors that govern these values. The most significant factors are the true radius evolution compared to the one determined from the PF analysis, the accuracy of the  $n_{532}$  and  $w_0$  parameters inferred from the fitting of  $Q_{\text{ext}}$  data sets to CSW Mie theory, fluctuations induced by vertical motions of the particle, and the uncertainties in  $\tau$ . Consider an ideal experiment in which the radius is exactly determined from the PF analysis, the particle is kept at a constant  $x$  and  $y$  position within the cavity standing wave and there is no uncertainty in  $\tau$ ; then, the  $n_{532}$  and  $w_0$  parameter space contains the exact values of the true particle RI and CRD beam waist. For such exact values, the percentage of points outside the envelope would be zero (perfect overlap). In the case of real measurements, when the determined radius,  $n_{532}$  and  $w_0$  are close to the true values,  $P_v$  is principally influenced by fluctuations in  $\tau_0$ . Domains can be seen in Figure 2 where the node and antinode CSW Mie simulations converge, and almost all the  $Q_{\text{ext}}$  data points fall outside the envelope in these regions. Therefore, there is a relationship between  $P_v$  and the fluctuations in  $\tau_0$  which can be quantitatively explored by simulation. From these HT measurements, the lowest achievable  $P_v$  for this single particle CRDS instrument was simulated to be around 23.8%. This simulation is for a particle with RI of 1.476 evaporating from a size of 2000–1000 nm and will depend on the particle radius range sampled and RI. The lower limit of the uncertainty (1 SD) in  $\tau_0$  was taken to be 0.2%. The simulated  $P_v$  for a well-behaved system in which there is no uncertainty in the RI provides a benchmark against which the best fits of  $Q_{\text{ext}}$  data sets for each studied particle can be considered individually.

The RI values for particles 1, 2, and 3, taken as the minima in  $P_v$  distributions, were determined as  $1.4792 \pm 0.0007$ ,  $1.4784 \pm 0.0002$ , and  $1.4781 \pm 0.0004$ , respectively. These three RIs, combined with the value determined for particle 4 ( $1.4775 \pm 0.0004$ ), yield an uncertainty-weighted mean of  $1.4782 \pm 0.0007$ . This RI value is higher than the value measured with the Misco refractometer (recorded as 1.476 at  $\lambda = 589$  nm) which is to be expected given the shorter wavelength of the single particle CRDS measurement. Ideally, the values obtained should be compared to refractometer values of the same wavelength, indicating whether the trapped particles contained a significant amount of water. Although the measurements were performed under dry  $N_2$  gas flow conditions, water is introduced into the cell on nebulization, as well as through atmospheric air leaking into the trapping cell chamber. These factors make lowering the in-cell RH below  $\sim 10\%$  experimentally challenging. The best fit  $w_0$  values of the individual measurements are  $276.4 \pm 0.4$ ,  $277.7 \pm 0.1$ , and  $282.9 \pm 0.1 \mu\text{m}$  for particles 1, 2, and 3, respectively, and compare favorably with the expectation of  $w_0 = 270.9 \mu\text{m}$  from Gaussian beam optics for a stable cavity of our design with perfect spherical mirrors. The variation in  $w_0$  from measurement to measurement most likely reflects minor changes in

optical alignment of our laser and cavity apparatus; consequently it is floated as a parameter in all fits, instead of constraining it to the expected value. Hereafter, we do not report the optimum fitted  $w_0$  values but note that they are always consistent with the expectation for our ring-down cavity.

The RIs of two PEG-400 particles were determined in the same way as for the HT particles. Figure 3 shows the measured

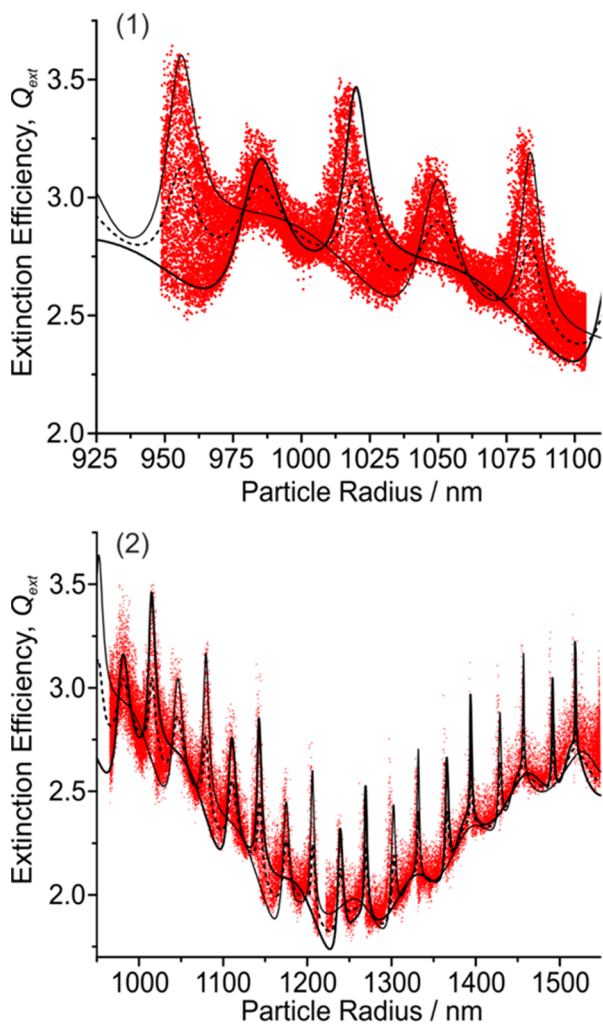


**Figure 3.** Measured  $Q_{\text{ext}}$  curves for PEG-400 particles 1 and 2 (red dots) as a function of radius are compared with CSW Mie calculations for a particle centered on a node (thin black line), an extremum (thick black line), and plane wave  $Q_{\text{ext}}$  simulation (dotted black line).

$Q_{\text{ext}}$  data with corresponding best-fit CSW Mie simulations. The best  $n_{532}$  values were determined to be  $1.471 \pm 0.004$  for particle 1 and  $1.476 \pm 0.002$  for particle 2. As with the HT particles, the determined  $n_{532}$  values are above the  $\lambda = 589$  nm RI of 1.467 (Misco refractometer) owing to the shorter wavelength used.

Despite the use of nitrogen purge flows and dust tubes, ambient dust entered the optical cavity during the measurements of PEG-400. These ambient particulates caused larger fluctuations in the  $\tau_0$  signal when compared to those obtained for the HT measurements, with percentage uncertainties in  $\tau_0$  of  $\pm 2\%$  and  $\pm 3.4\%$  for particles 1 and 2 respectively (compared with  $\tau_0$  uncertainties  $< 1\%$  for the HT particles). This increased experimental noise manifests in the  $Q_{\text{ext}}$  plots as a larger

number of data points lying outside the CSW Mie simulation envelope when compared to the HT measurements. The minima in  $P_v$  are unsurprisingly at higher percentages than typical values obtained from HT data (42.4% and 58.1% for particles 1 and 2 respectively) and contribute to the higher uncertainties in the determined  $n_{532}$ . Despite this higher  $P_v$  compared to the HT measurements, the RIs for the two PEG-400 particles agree within the precision of the measurement. These data demonstrate that, in future measurements, the noise in  $\tau_0$  should be kept  $< 1\%$  to obtain high precision RI determinations with percentage uncertainties  $< 0.1\%$ .

We thus establish that, under favorable experimental conditions, RIs for single-component particles can be measured to high precision (within  $\pm 0.3\%$ ) and with good reproducibility (within  $\pm 0.4\%$ ). However, the particles used were of low volatility and the effects of higher volatility composition are explored in the next section.

**III.b. Accuracy in RI Determination for Droplets of High Volatility.** High volatility droplet components limit the time over which CRDS measurements of extinction can be made, and the number of measurements accumulated at any particular droplet radius. Maintaining precise levitation of a rapidly evolving droplet at the center of the ring-down cavity is also difficult because of short-time changes to the particle's light-scattering properties. Both these effects have consequences for the precision of single-particle RI determination, as illustrated in this section for glycerol droplets.

A rapidly evaporating glycerol particle was trapped, and the time evolution of the radius and  $\tau$  values were recorded (Figure 4a and b, respectively). The RH of the cell during evaporation was, on average,  $\sim 10\%$ . The RI of the particle at this RH was estimated to be 1.470 using a mass weighted linear mixing rule and the Aerosol Inorganic–Organic Mixtures Functional groups Activity Coefficients (AIOMFAC) model, and this RI was used in the fitting of the phase functions.<sup>30</sup> The average rate of radius change,  $dr/dt$ , of glycerol was determined to be  $-2.1 \pm 0.2 \text{ nm s}^{-1}$ , which is much higher than that for measurements involving either HT ( $\sim -0.1 \text{ nm s}^{-1}$ ) or PEG-400 ( $\sim -0.05 \text{ nm s}^{-1}$ ). The radius evolution is observed to slow toward the end of the measurement, most likely because of a rise in impurity concentrations as the more volatile components of the particle evaporated. The BB laser intensity feedback struggled to compensate for the rapidly changing radiation pressure efficiency of the evaporating particle. The response of the feedback system was limited by a combination of the maximum frame rate of the CMOS camera (DCC1545M) and the data-acquisition computer processing power. Hence, excursions in particle position of  $> 200 \mu\text{m}$  (Figure 4c) were observed at radii where the particle scattering was resonant with the laser light. Large excursions in the particle position along the length of the BB (thus transverse to the axis of the CRD beam) led to sudden increases in  $\tau$  and hence sharp dips in apparent  $Q_{\text{ext}}$  values. Although these excursions did not affect the size determination from PF measurements they made precise  $\sigma_{\text{ext}}$  measurements difficult.

The underlying interference structure of the measured  $Q_{\text{ext}}$  and CSW Mie simulations can be compared for different simulated RIs. The broad oscillations apparent in the RDT data are a result of the changing interference between light transmitted through and passing around the particle. The phase delay of the transmitted light depends on the particle radius, RI, and illuminating wavelength. Given that the radius range covered by this evaporating glycerol particle is large

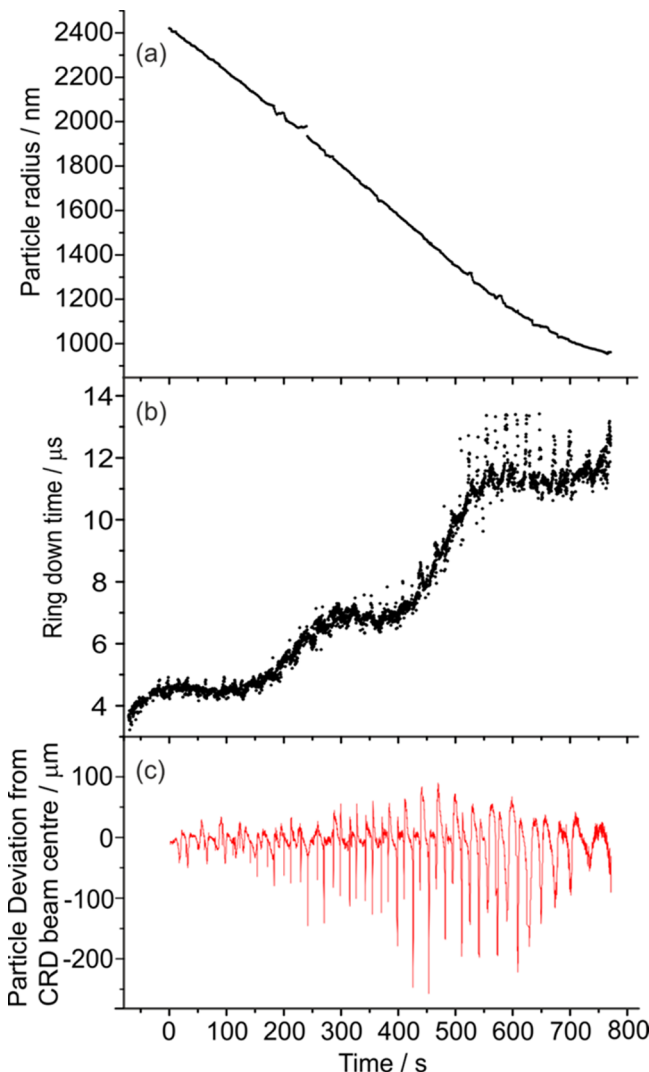


**Figure 4.** (a) Radius as a function of time for an evaporating glycerol particle. The initial time when PFs are recorded is denoted as  $t = 0$  s. (b) Variation of the RDT for the evaporating glycerol particle. (c) PF image position variation over the course of the measurement. A positive deviation from the beam center indicates an increase in particle height.

( $\sim 1500$  nm), the interference structure of the measured and simulated  $Q_{ext}$  can be compared to provide a reasonable estimate of particle RI. The RI of the droplet in CSW Mie calculations was varied in increments of 0.001 and an RI of  $n = 1.455$  was estimated from the best agreement between measured and simulated oscillations, as shown in Figure 5. The  $270.9 \mu\text{m}$  beam waist used in the simulations is that expected for the geometry of the optical cavity. The vertical displacement of the experimental and simulated data shows that this beam waist is a slight underestimate, but this does not affect the conclusions regarding RI values. Simulated plots with RI values 0.02 greater or smaller than the best fit value are included in Figure 5 to demonstrate the poor agreement they give between the measured  $Q_{ext}$  and CSW Mie simulations. It is difficult to assess the accuracy of the RI determined because of the scatter in the  $Q_{ext}$  data, although it is clear that an RI of 1.455 for the CSW Mie simulations gives much better agreement than RI values of 1.435 or 1.475.

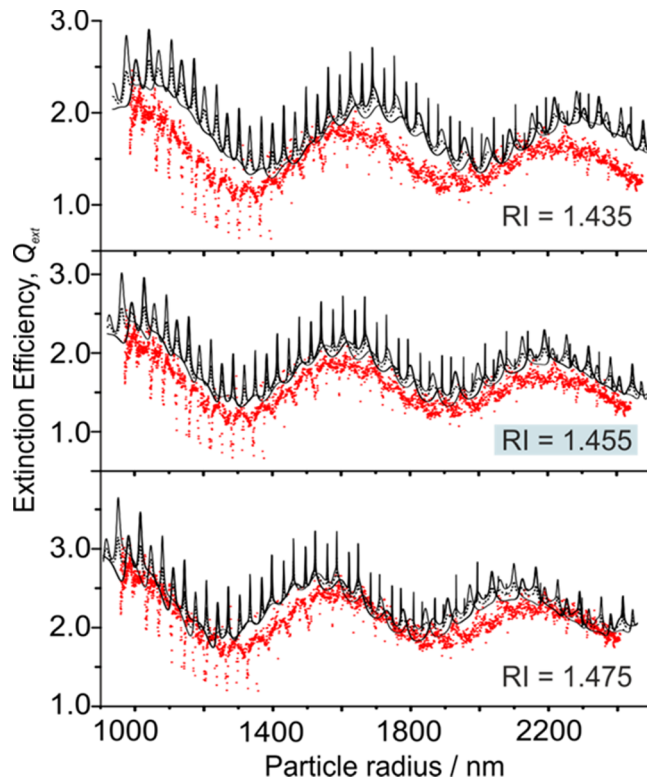


**Figure 5.** Measured  $Q_{ext}$  values (red dots) for the evaporating glycerol particle are compared with simulated  $Q_{ext}$  values obtained using different RIs. The middle panel shows the best fit chosen by varying the RI so that the underlying interference structures in  $Q_{ext}$  align.

The RI determined for glycerol is  $1.455 \pm 0.02$ , which is lower than the value of  $1.4746 (\lambda = 532 \text{ nm})$  for the pure liquid.<sup>31</sup> This difference in RI may be a result of the water content of the particle being higher than expected from the RH measurement. Using the AIOMFAC model to estimate composition, an RI of 1.470 at 10% RH is predicted and is within the uncertainty of our determined RI, while the measured RI of 1.455 would correspond to an in-cell RH of  $\sim 44\%$ . The RH probe is situated at the wall of the cell,  $\sim 1 \text{ cm}$  from the location of the droplet. It is possible that the RH at the position of the droplet is larger than that measured at the RH probe, but a difference in RH of  $>30\%$  is unlikely. An alternative explanation is that there are hygroscopic impurities in the sample that affect the RI. Figure 4a shows that  $dr/dt$  decreases toward the end of the measurement, hinting that impurities may be present in the particle. If the overall RI of the impurities were less than that for glycerol, we would measure a lower RI.

The general conclusion from the results presented in this section is that high evaporation rate of a droplet gives poor quality single-particle RDT data and there is a resulting large uncertainty in the determined RI. Nevertheless, despite the lower accuracy of the retrieved RI compared to the less volatile organic aerosol particles considered in section III.a, this accuracy is still comparable to that achieved by ensemble cavity ring-down measurements.<sup>9</sup>

#### IV. MEASUREMENT OF HYGROSCOPIC INORGANIC AEROSOL OPTICAL PROPERTIES

We now compare the measured  $Q_{ext}$  data for hygroscopic inorganic particles to CSW Mie simulations which employ the

parametrizations of Tang and co-workers to relate the RI to the particle radius.<sup>21</sup> Trapped aqueous droplets are exposed to a reduction in ambient relative humidity and consequent evaporation of water causes a decrease in the particle radii and changes in composition and RI. The main purpose of the work presented in this section is to test the single-particle CRDS measurements for two-component aqueous droplets against established models of variation of RI with size and ambient RH. We use atmospherically relevant ammonium bisulfate and sodium nitrate aerosol droplets. The SN data are compared to our previous measurements using ensemble cavity ring down spectroscopy and optical tweezers, which verified the accuracy of the parametrizations by Tang and co-workers. Further tests are then presented using aqueous ammonium sulfate and sodium chloride aerosols. The former system is used to examine the reproducibility of measurements over cycles of increasing and decreasing RH, and consequent hygroscopic growth and evaporation. It also presents an opportunity to investigate whether particles trapped for extended periods take up impurities, such as contaminant volatile compounds other than water.

**IV.a. Refractive Index Treatments for Aqueous Inorganic Salt Droplets.** This subsection focuses on the determination of RI changes with RH for aqueous inorganic salts for which the literature already contains parametrizations against which our measurements can be tested. For hygroscopic aerosol, a relationship between RH and RI can be used to characterize the composition of the particle as the measured in-cell RH changes. The variations of RI with RH for many aqueous inorganic aerosol species are known from the studies of Tang and co-workers.<sup>21,23,24,32</sup> Solute concentrations,  $c$ , are related to water activity,  $a_w$ , via eq 3, and the concentration to RI through eq 4. We will refer to these expressions as the Tang parametrizations.

$$c(a_w) = A_1 a_w + A_2 a_w^2 + A_3 a_w^3 + A_4 a_w^4 \quad (3)$$

$$n(c_i) = B_1 c_i + B_2 c_i^2 + B_3 c_i^3 + B_4 c_i^4 \quad (4)$$

$A_n$  and  $B_n$  are polynomial coefficients which are tabulated in the papers of Tang and co-workers. When determining the radius from an experimental PF, there are two ways in which the RI for each Mie generated PF can be approximated. The most direct method is to relate the RH associated with each experimental PF to an RI using the Tang parametrizations as described in eqs 3 and 4, assuming the RH to be equal to the value reported by the in-cell capacitance probe. This method has an experimental limitation: the response time of the in-cell RH probe to changes in the gas phase water composition can differ from the response time of the particle radius. A solution to this problem, the second approach, is to trap the particle at a constant high RH for a significant time period ( $>10$  min) to ensure the gas phase RH at the capacitance probe and at the droplet position are equal. This equilibrium point is termed the initial time point,  $t_0$ , at which the particle RI can be calculated through the Tang parametrizations and the measured RH, allowing a determination of initial radius,  $r_0$ , from the measured PF. As the RH is lowered, an assumption of volume additivity is made; the total volume of inorganic solute is invariant with the changing droplet radius. Accordingly, for any given radius,  $r$ , the concentration is given by eq 5, where  $c_0$  is the concentration of the particle at the initial time point,  $t_0$ .

$$c(r) = \left( \frac{r_0}{r} \right)^3 c_0 \quad (5)$$

Equations 4 and 5 allow a RI to be estimated for any particle radius once  $r_0$  is determined, giving a RI/radius relationship. The RIs used by Tang and co-workers were measured at a wavelength of 632.8 nm and a correction for wavelength dispersion must be applied using coefficients given by Millard and Seaver for seawater, the best available approach.<sup>33</sup> Once the radius is determined from the PF, the measured  $Q_{ext}$  of the particle can be inferred for each optical cross-section measured by CRDS. The RI/radius relationship used in determining the radius from the PF is also used in calculation of the CSW Mie scattering envelope. Here, the two parameters  $w_0$  and radius offset are varied, while it is no longer appropriate to vary  $n_{532}$  as this is predetermined by the Tang parametrizations. We now report the resulting measured  $Q_{ext}$  for hygroscopic growth experiments on various aqueous inorganic aerosol species, investigating the agreement with CSW Mie theory when the Tang parametrizations are used to describe the RI. These measurements provide a way of validating the RH-dependence of the Tang parametrizations through examining the consistency of our CRD measurements and CSW predictions. In this paper, we do not discuss the possibility of using the measurement to directly retrieve RI values without reference to a pre-existing model.

**IV.b. Ammonium Bisulfate.** Our measurements on ammonium bisulfate reported in this subsection demonstrate that the Bessel-beam trapping and single-particle CRDS technique can be applied to particles of radius  $<1\text{ }\mu\text{m}$ . Figure 6 panels a and b respectively show the changing radius and RDT for an evaporating aqueous AB particle. The RI/radius relationship for the particle, as determined using the initial in-cell RH (at  $t_0$ ) and the Tang parametrizations, is given as an inset in Figure 6a. This particle evaporates from a radius of  $\sim 970$  to  $\sim 730$  nm, within the fine mode regime that is relevant for atmospheric optics.

The particle radius was converted into a geometric cross-section and the  $Q_{ext}$  was then determined from the CRD data. CSW Mie simulations of  $Q_{ext}$  using the RI/radius relationship shown in Figure 6a are compared with the measured  $Q_{ext}$  in Figure 6c and the minimum value of  $P_v$  is determined to be 39.5%. The agreement between the experimental  $Q_{ext}$  and simulated curves based on the Tang parametrizations is mostly good but there is some disagreement at low particle radii.

The discrepancy between measurements and simulation at small particle radii derives from the rate of change of radius,  $dr/dt$ , which varies over time. Figure 6a shows that this rate is lower at the start of the measurement than at the end. For the first 4500 s and for the last  $\sim 3000$  s, the values of  $dr/dt$  are  $-8.3 \times 10^{-3}$  and  $-21.2 \times 10^{-3}\text{ nm s}^{-1}$ , respectively. The acquisition rate of RDT data is constant over the entire experiment, which means that the density of  $Q_{ext}$  measurements for a given radius, which we denote  $\rho(r)$ , is higher for radii between 975 and 930 nm (where the radius changes more slowly) than for measurements at lower radii. Values for  $\rho(r)$  of  $420$  and  $117$  points  $\text{nm}^{-1}$  are determined for the first 4500 s and final  $\sim 3000$  s, respectively. This change in  $dr/dt$  highlights a shortcoming in our current method of quantifying the agreement between the measured  $Q_{ext}$  and the CSW Mie simulations and suggests scope for improvements to be implemented in future analyses; fits may be biased toward regions of  $Q_{ext}$  data where  $\rho(r)$  is higher. The changing  $dr/dt$

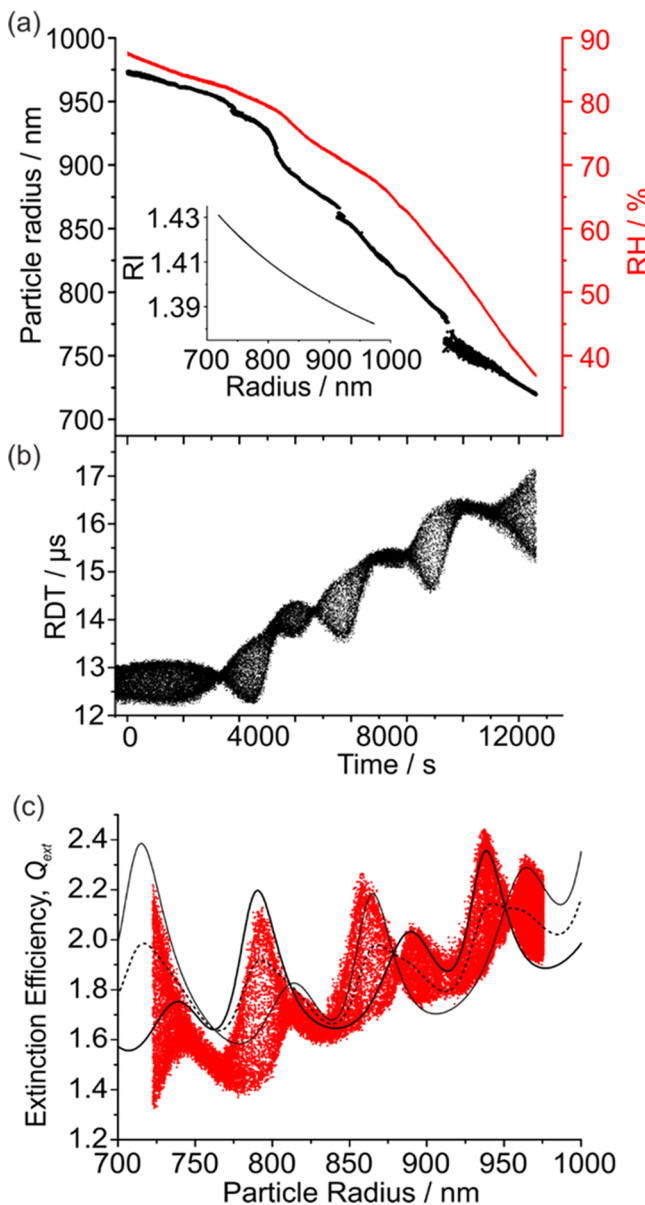


**Figure 6.** Changes in particle radius, experimental ring-down, and extinction efficiency with time for an evaporating AB particle. (a) Radius and RH variation with time. The inset shows the RI/radius relationship used in radius determination. (b) RDT variation with time for the shrinking particle. (c) Measured  $Q_{ext}$  (red data points) for the AB particle. The solid black lines indicate the CSW Mie simulations for the particle centered on a node or antinode, whereas the dashed line indicates a conventional Mie simulation.

does not cause the disagreement between the CSW simulated and experimental  $Q_{ext}$  but it does bias the fitting toward the higher radii. The disagreement between CSW Mie simulations and experimental data could instead be the result of either the Tang parametrization being subtly incorrect for AB, or the RH probe giving an erroneous reading, thus giving an incorrect initial concentration  $c_0$ .

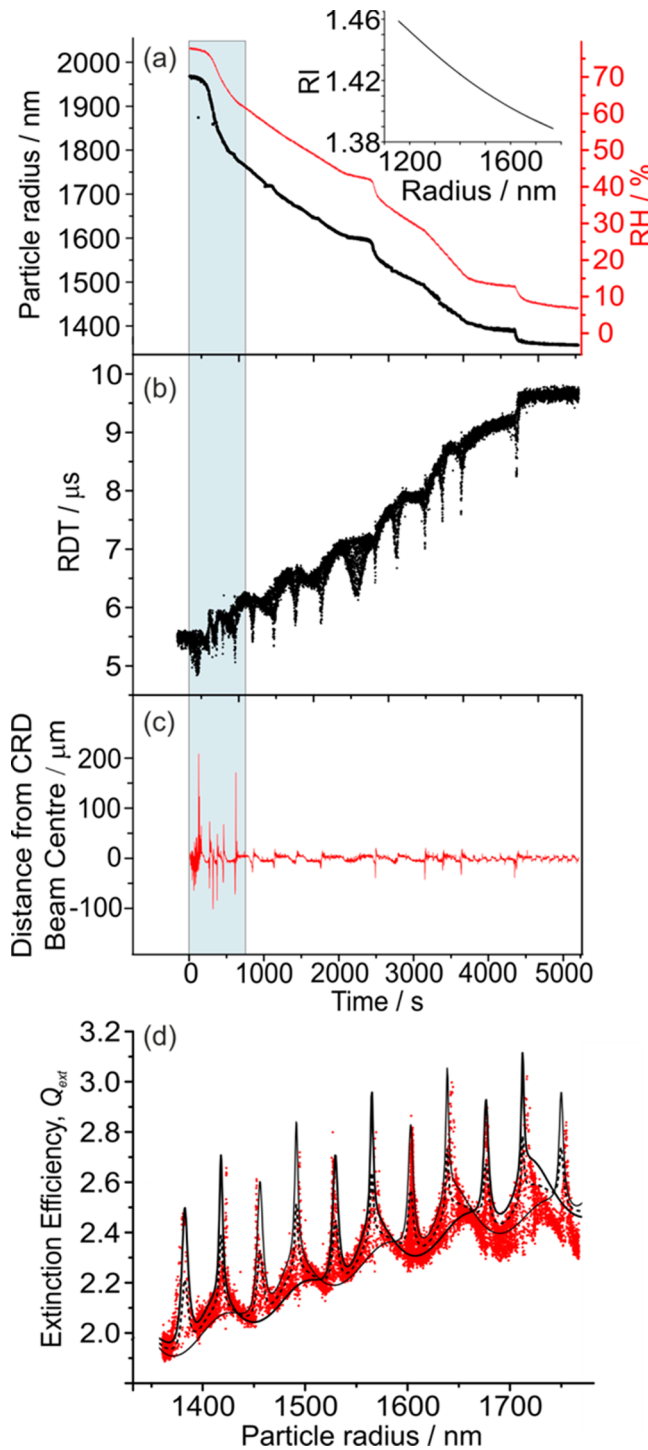
**IV.c. Sodium Nitrate.** The study of sodium nitrate presented in this subsection provides a test case for our methods using a sample with a well-characterized RI variation during hygroscopic size change. In a study of SN particles by Mason et al., the RI calculated at  $\lambda = 632$  nm from the parametrization provided by Tang was found to agree very

favorably with measurements made using optical tweezers ( $\lambda = 650$  nm) over a range of RH values and reasonably well with measurements made using ensemble CRDS ( $\lambda = 532$  nm).<sup>9</sup> Typical uncertainty in the RIs from the ensemble CRDS measurements was  $\pm 0.02$ , which is much higher than the measured uncertainty in RIs of  $\pm 0.004$  from the optical tweezers measurements. In addition, the latter method allowed measurements of the RI of SN droplets down to 16% RH without efflorescence.

Figure 7 reports the hygroscopic response of a SN particle, trapped initially at an RH of  $\sim 80\%$ , which eventually fell from the trap when the RH was lowered to 6%. When a particle is trapped using the BB, efflorescence is usually accompanied by distortions of the PF or ejection of the particle from the trap. No distortions were observed in the PF images, suggesting no efflorescence occurred even at low RH, consistent with the findings in our prior optical tweezers study. In section III.b, measurements on a glycerol particle showed that at particle evaporation rates of  $2 \text{ nm s}^{-1}$  or greater, excursions of the particle along the length of the BB were too rapid for the laser feedback to compensate adequately. A time period is highlighted in Figure 7a–c during which the rate of change of SN particle radius was  $1\text{--}2 \text{ nm s}^{-1}$ , causing the particle to move significantly within the CRD beam, as shown in panel c. The RDT data in this highlighted time period were therefore excluded from the final  $Q_{ext}$  fitting. The final 700 s of RDT data were also excluded because  $\rho(r)$  is significantly higher than at earlier times and so may bias the  $Q_{ext}$  comparison. Figure 7d shows the best fit  $Q_{ext}$  for the SN particle, for which the minimum in  $P_v$  was 34.4%. The resonance structure and the underlying contour of the changing  $Q_{ext}$  agree well with the CSW Mie simulations, indicating that the RI and radius have been well-determined throughout most of the hygroscopic size change. Given that the optical tweezers measurements showed the Tang RI/concentration parametrization to be accurate for SN, it is probable that the deviations at high radii result from limitations in the accuracy of the RH probe.

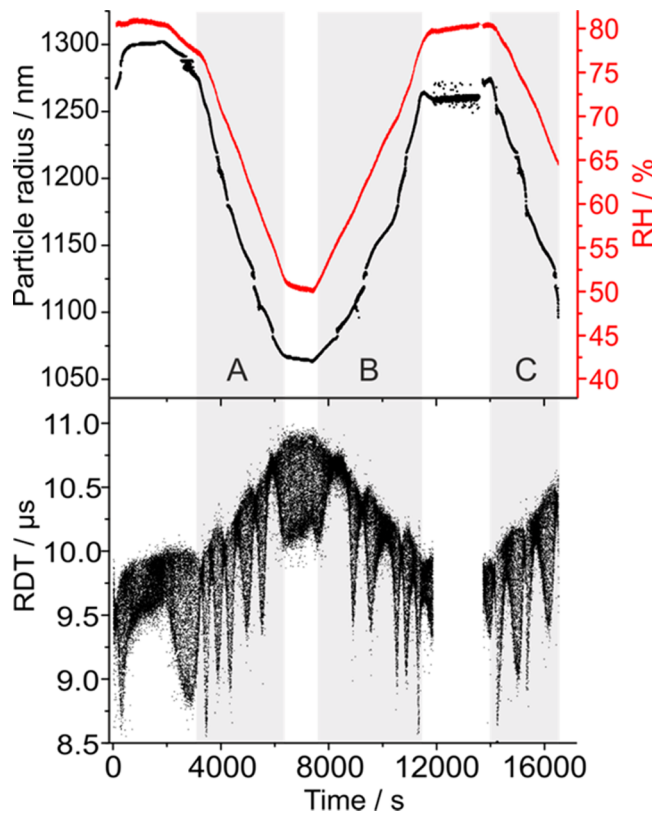
**IV.d. Ammonium Sulfate.** Studies were conducted on AS particles to compare the reproducibility of measured  $Q_{ext}$  data over repeated hygroscopic growth and evaporation cycles. The calculation of the particle  $\sigma_{ext}$  uses an interpolated value of  $\tau_0$  and we assess whether this background RDT drifts over the course of such extended measurement of  $Q_{ext}$ . These studies were performed by cycling the RH and comparing the measured  $Q_{ext}$  during evaporation and condensation cycles.

Figure 8a shows the radius variation for an AS particle undergoing evaporation (labeled region “A” in the figure), condensation (“B”), and then evaporation again (“C”) as the RH was varied between 80 and 50%. The accompanying variation in RDT is shown in Figure 8b. The measured RDT patterns are visibly symmetric about the evaporation/condensation cycle changes. A portion of the RDT data between B and C is omitted because  $\tau_0$  was remeasured during this period by moving the particle out of the CRD beam. The determination of the particle radius is unreliable during this period because the PF of the displaced particle was not entirely collected by the camera. During each evaporation and condensation cycle, discontinuities were observed in the radius data, particularly in the final evaporation step, C. These discontinuities are an artifact of the PF fitting arising from experimental noise in the PF (from objective aberration, solute deposits on optics), assuming plane wave illumination of the droplet, and subtle misassignments of the angular range and RI.



**Figure 7.** (a) Determined radius and RH for a SN droplet, with an inset that shows the RI/radius relationship used in the PF analysis. (b) Measured RDTs. (c) Position of droplet with respect to the center of the CRD beam. A portion of the data is highlighted in which the radius change is rapid, causing significant vertical motion of the particle along the length of the BB. (d) Measured (red dots) and simulated (black lines)  $Q_{ext}$  values for the SN particle.

Initially, when comparing the  $Q_{ext}$  data to CSW Mie simulations, both  $w_0$  and a radius offset were treated as fitting parameters. When fitting the radius offset, large negative values of  $-5$  and  $-7$  nm were obtained for regions A and B. Subsequent comparison of the best-fit  $Q_{ext}$  measurements to CSW Mie simulations showed that the positions of the



**Figure 8.** Radius, RH, and ring-down time of an AS particle in a changing RH environment. The top panel shows the RH changes with time (red) and associated particle radius changes (black) deduced from PF fitting. The lower panel shows changes to the RDT as the particle size changes. The gap in the ring down time data starting at  $t = 12\,000$  s results from the particle being moved vertically out of the ringdown beam to remeasure  $\tau_0$ .

simulated and experimental resonance peaks were offset by as much as 20 nm, which is much larger than offsets seen in the other data sets presented here (1–2 nm difference). The larger offsets for the current AS data may be a consequence of biased fitting toward the regions of high  $\rho(r)$  at the lowest radii. Thus, a radius offset was not applied and the  $Q_{ext}$  data were instead fitted to CSW Mie simulations by varying  $w_0$  only. Figure 9 shows the best-fit  $Q_{ext}$  measurements with corresponding CSW Mie simulations for the evaporation and condensation cycles A–C. The best fit returned  $P_v$  values for A–C of 36.5%, 30.0%, and 38.5%, respectively. From both  $P_v$  values and by visual inspection, the agreement between simulated and measured  $Q_{ext}$  is good, verifying that the Tang parametrizations are accurate for the treatment of RI for aqueous AS aerosol particles. The correspondence between simulations and measurements in plots of  $Q_{ext}$  in Figure 9 makes clear that  $\tau_0$  does not significantly drift during the time periods in which  $\tau_0$  is not being measured.

**IV.e. Sodium Chloride.** In experiments on aqueous droplets containing inorganic solutes, lowering the RH increases the solute concentration as water evaporates and may result in efflorescence. A particle trapped in a Bessel beam is typically ejected from the optical trap when it effloresces. The phase function obtained just prior to particle ejection provides the particle radius and can be matched to the particular RH value corresponding to particle loss. If we take this RH to be the efflorescence RH (ERH), we can in principle establish the

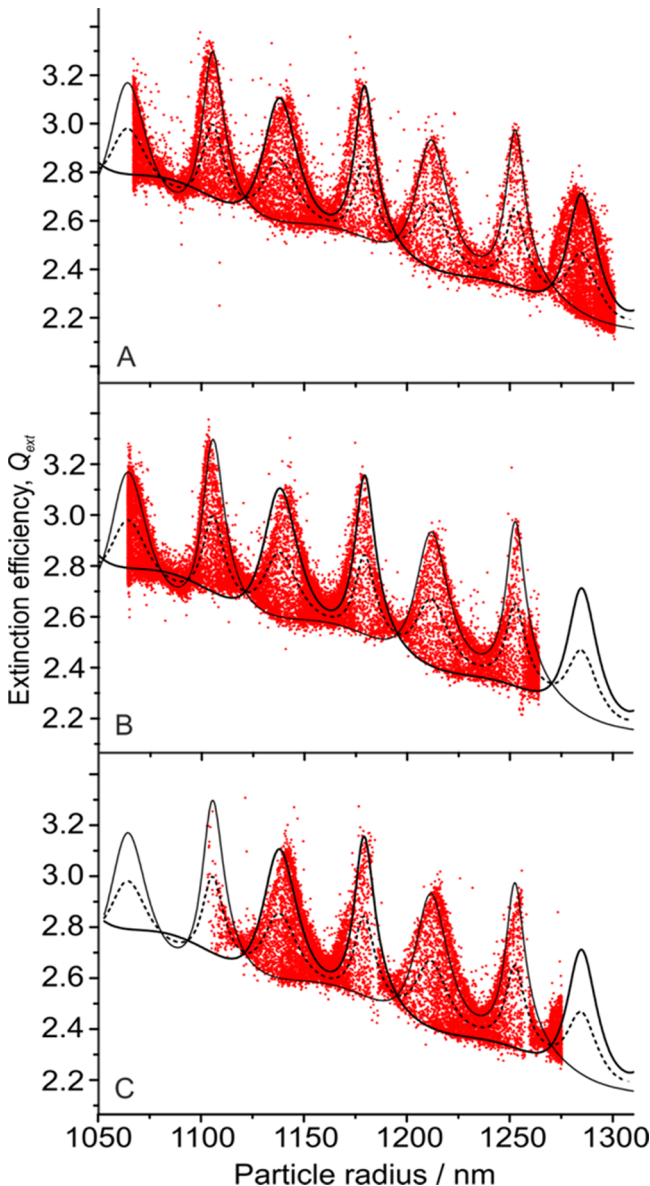


**Figure 9.** Extinction efficiency plots for the AS particle featured in Figure 8 during time periods A–C. In each case the RI/radius relationships for the simulated  $Q_{\text{ext}}$  plots are the same as used in the fitting of the phase function data. The radius offset used in each case was set to 0 nm.

full RI/radius relationship for higher RHs. The final example presented tests the reliability of this approach, and contrasts with most of our measurements where we take the initial upper limit on the RH as the reference point for all subsequent data. It uses an aqueous sodium chloride droplet subjected to decreasing RH until the particle falls from the BB trap. In the SC measurements presented, the solute concentration of a solution droplet was determined using eq 5, and the literature ERH, with the PF just prior to trap loss analyzed in combination with RI values from the Tang parametrization of eq 4 to size the pre-efflorescence droplet. The ERH of SC is predicted to be 45–46% by Gao et al., which is in good agreement with experimentally measured ERH values.<sup>34,35</sup>

The SC particle was observed to exit the trap when the RH probe read 54% RH, which is significantly higher than the expected ERH and may indicate trap loss before efflorescence.

Thus, three RHs between the measured and expected ERH were chosen (55, 50, and 45%) and the corresponding RI/radius relationships calculated. Figure 10 shows the time-

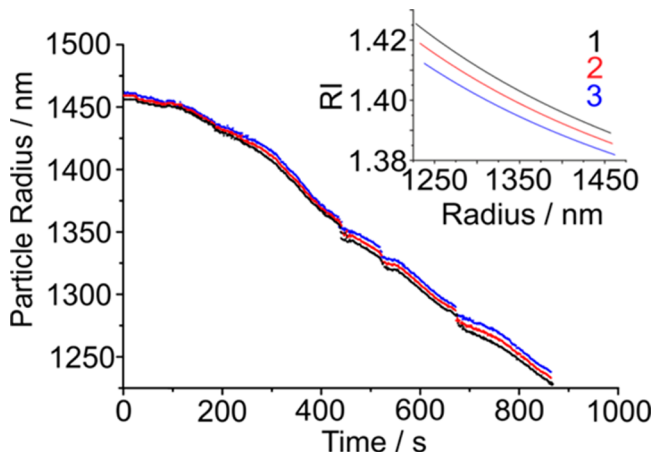


**Figure 10.** Particle radius determined using three different RI/radius relationships based on the RH at which the particle effloresces: 45% (treatment 1, black); 50% (treatment 2, red); 55% (treatment 3, blue). (inset) RI/radius relationship used in each radius determination.

dependent radii obtained from the PF fitting of a SC particle using the three different RI/radius treatments shown in the inset. The offsets between the radii obtained using each of the RI treatments are 5 nm. The first 150 s of points in the radius-time plots were excluded from the analysis of  $Q_{\text{ext}}$  to avoid a fitting bias from a changing  $\rho(r)$ . The time-dependent radius of the particle was also estimated using the approximation of a fixed RI, with a value of 1.4 chosen because it is central to the expected range.

Measured  $Q_{\text{ext}}$  and corresponding best-fit CSW Mie simulations are shown in Figure 11 for these four adopted RI treatments. The agreement between the measured  $Q_{\text{ext}}$  and the CSW Mie simulations is much better when the Tang RI/radius relationship is used than when a constant RI is chosen. This qualitative observation is supported by a minimum  $P_v$  value of 50.7% for the constant RI fit which is approximately double that obtained when using one of the Tang treatments. The quality of the fits using the Tang parametrization cannot be distinguished simply by inspection of the  $Q_{\text{ext}}$  envelopes. Instead, we refer to the minimum  $P_v$  values for treatments labeled 1–3 in Figure 11 of 25.9, 23.5, and 23.0%, respectively. Thus, treatment three gives a representation of the RI/radius that best matches the experimental  $Q_{\text{ext}}$  data, corresponding to a lowest RH value for this set of measurements of 55%. This value compares well with the final measured RH value from the probe of 54% but is significantly different from the literature ERH value of 45%. The likely explanation for this discrepancy is that the particle was ejected from the trap before it effloresced. Further analysis must be performed to determine whether or not such a difference in the minima in  $P_v$  for the three RI/radius relationships is significant. However, it is clear that assuming the literature value for the ERH at the point of particle loss from the trap may provide a poor reference point for analyzing the optical data. Care must be taken in applying the suggested strategy for use of ERH data; true efflorescence of the particle, not simply trap loss, must be established first. Nevertheless, consistency is once again observed between the measured and simulated extinction efficiencies when the Tang

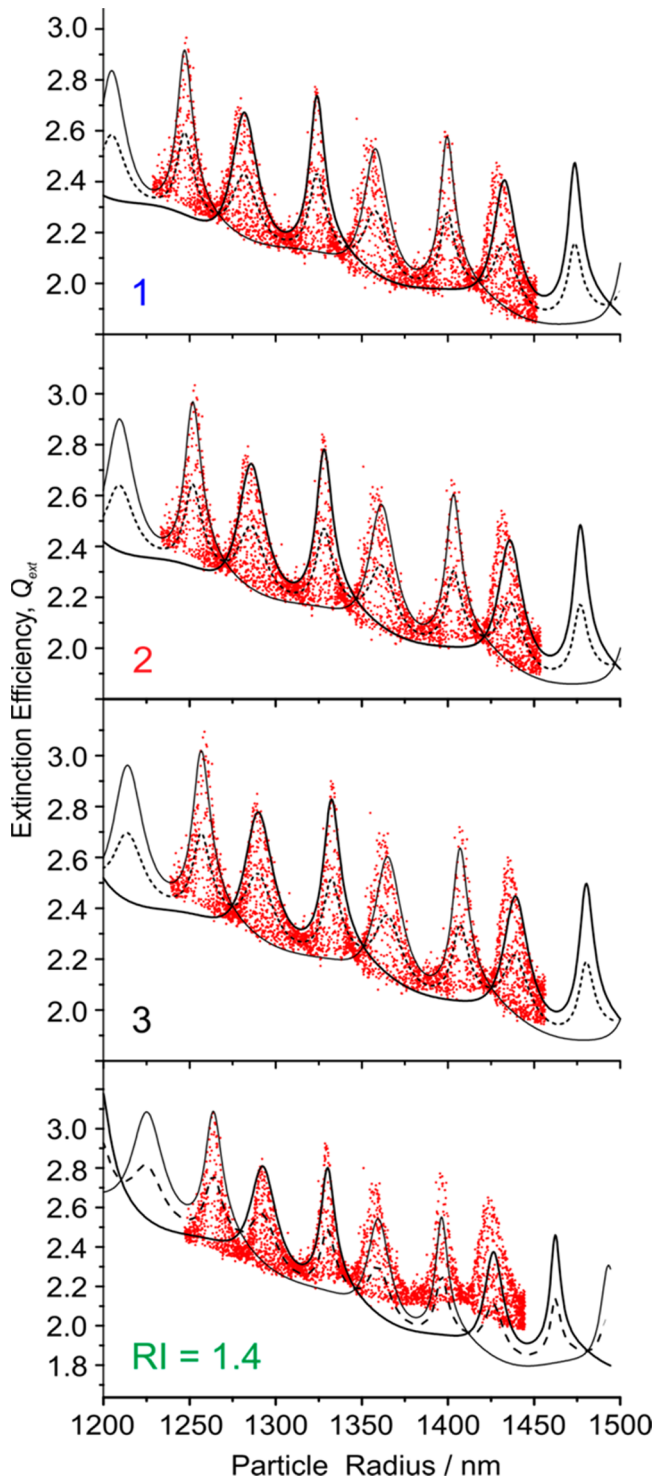


**Figure 11.** Extinction efficiency analysis for an aqueous SC particle. Red dots are  $Q_{\text{ext}}$  values deduced from CRDS measurements and black lines are CSW Mie simulations using four different treatments of the RI. The top three panels are for treatments 1–3 (see Figure 10), and the bottom panel is for a fixed RI of 1.4.

parametrization of RI is used with the RH reference point determined from the in-cell capacitance probe.

## V. CONCLUSIONS

The single particle CRDS technique for measuring  $Q_{\text{ext}}$  of organic and aqueous inorganic particles has been tested by

comparison of measurements with CSW Mie theory simulations of  $Q_{\text{ext}}$  envelopes. The scope and limitations of this technique for RI measurements for volatile organic species have been characterized and RI variations reported for droplets of various compositions that evolve over time. The power of this new technique for determining the extinction cross sections and RIs of single particles of changing composition and/or size has been demonstrated. Application of the method can be extended to the study of single particles of any atmospherically relevant composition provided that it the particle does not significantly absorb at the BB trapping wavelength of 532 nm.

The RI of HT was measured as  $1.47824 \pm 0.00072$ , which is larger than a  $\lambda = 589$  nm refractometer value of 1.476, consistent with typical RI dispersion trends for most substances in the visible spectrum. Measurements for PEG-400 particles demonstrated that fluctuations of  $\pm 2\%$  or more in  $\tau_0$  will decrease the precision of the RI measurement, and thus  $\pm 1\%$  uncertainty is recommended as the upper limit to enable precise analysis of single particle CRDS measurement. When semivolatile organic particles evaporate too fast for the laser feedback to compensate adequately for changes in the droplet's radiation pressure efficiency, there is poor particle confinement within the CRD beam center. Large excursions of the particle lead to poor RI determination. Instead, the RI may be estimated by matching the broad oscillations in the interference structure of  $Q_{\text{ext}}$  as the droplet changes size to the shape of the CSW Mie simulations. The upper limit on the uncertainty in the RI determined in this way is  $\pm 0.02$ , which is similar to the RI uncertainty typical for aerosol ensemble CRDS measurements.<sup>8</sup> Extinction measurements on glycerol droplets suggested that an upper limit for the rate of size change of  $2 \text{ nm s}^{-1}$  should be used for this instrument. This limit is imposed by a combination of the frame rate of the phase function acquisition camera (13 Hz) and computational processing power of the data-acquisition computer. RI measurements presented here demonstrate that the radius measurement made by analysis of the PF has a precision of better than 5 nm when the angular range and RI are correctly assigned.

$Q_{\text{ext}}$  values for selected aqueous inorganic particles were determined as a function of their changing radius as the ambient in-cell RH was varied. The measured in-cell RH was used in conjunction with the parametrizations of Tang and co-workers linking RI to water activity to estimate droplet radius as a function of RH from the PF measurements. Then, consistency between measured extinction efficiencies and CSW predictions can be taken as confirmation of the validity of the RH-dependence of the Tang parametrizations. In addition, measurements with an AS particle over repeated cycles in RH confirmed the reproducibility of measurements during droplet evaporation and condensation. For aqueous AB particles, the agreement between measured and CSW simulated  $Q_{\text{ext}}$  envelopes is not as good as for SN, AS, and SC particles. The presence of impurities or bisulfate in the AB sample could explain this discrepancy. However, if we assume that the sample was pure, two further possibilities may instead explain this difference. First, the Tang parametrizations may not accurately provide a relationship between RH and RI for AB as a result of inaccuracies in the coefficients of eqs 3 and 4. Second, the RH probe for these measurements may not have given a good indication of the water activity in the vicinity of the droplet at the initial time point,  $t_0$ . It should be remembered, however, that good agreement is observed for the SN, AS, and SC

measurements using the values reported by the RH probe. A more comprehensive study is required that provides determinations of RI independently of an assumed treatment such as those of Tang; this will be the focus of a subsequent approach.

For each inorganic system, variation in the rate of change of droplet radius may induce bias in the fitting of  $Q_{ext}$  data to CSW Mie simulations. Binning the measured  $Q_{ext}$  data into small radius intervals, and weighting points outside the CSW-Mie envelope by division by the number of points in the appropriate size bin should eliminate this bias. This method will be implemented in future studies that seek to determine unknown RI/composition relationships. Measurements performed on an aqueous SC particle show the effect of varying the RI/radius relationship on the agreement between measured and simulated  $Q_{ext}$  values, as quantified by the parameter  $P_v$ . Although  $P_v$  varies with the RI/radius description used, the variation in  $P_v$  is small. It is unclear whether such a small variation is significant enough to conclude that the simulation giving the lowest  $P_v$  is the best choice. Ultimately, the single particle CRDS technique would be improved if the RI were fitted for both the PFs and measured  $Q_{ext}$  data in a self-consistent way, independent of any literature parametrizations. This approach will be the subject of a forthcoming publication.

## AUTHOR INFORMATION

### Corresponding Author

\*E-mail: j.p.reid@bristol.ac.uk.

### Notes

The authors declare no competing financial interest.

## ACKNOWLEDGMENTS

J.P.R. acknowledges financial support from the EPSRC through a Leadership Fellowship (EP/G007713/1) and B.J.M. thanks the EPSRC for funding. M.I.C. acknowledges funding from NERC and the RSC through an Analytical Trust Fund studentship and support from the Aerosol Society in the form of a CN Davies award. We thank NERC for the award of grant NE/H001972/1 that supported instrument development.

## REFERENCES

- (1) Seinfeld, J. H.; Pandis, S. N. *Atmospheric Chemistry and Physics - From Air Pollution to Climate Change*, 2nd ed.; John Wiley & Sons, Ltd: New York, USA, 2006.
- (2) Hoffman, R. C.; Laskin, A.; Finlayson-Pitts, B. J. Sodium Nitrate Particles: Physical and Chemical Properties during Hydration and Dehydration, and Implications for Aged Sea Salt Aerosols. *J. Aerosol Sci.* **2004**, *35*, 869–887.
- (3) Finlayson-Pitts, B. J.; Pitts, J. *Chemistry of the Upper and Lower Atmosphere*; Academic Press, 1999.
- (4) Finlayson-Pitts, B. J.; Hemminger, J. C. Physical Chemistry of Airborne Sea Salt Particles and Their Components. *J. Phys. Chem. A* **2000**, *104*, 11463–11477.
- (5) Zhang, Q.; Jimenez, J. L.; Canagaratna, M. R.; Allan, J. D.; Coe, H.; Ulbrich, I.; Alfarra, M. R.; Takami, A.; Middlebrook, A. M.; Sun, Y. L.; et al. Ubiquity and Dominance of Oxygenated Species in Organic Aerosols in Anthropogenically-Influenced Northern Hemisphere Midlatitudes. *Geophys. Res. Lett.* **2007**, *34*, 1–6.
- (6) Hasenkopf, C. A.; Beaver, M. R.; Trainer, M. G.; Langley Dewitt, H.; Freedman, M. A.; Toon, O. B.; McKay, C. P.; Tolbert, M. A. Optical Properties of Titan and Early Earth Haze Laboratory Analogs in the Mid-Visible. *Icarus* **2010**, *207*, 903–913.
- (7) Pettersson, A.; Lovejoy, E. R.; Brock, C. A.; Brown, S. S.; Ravishankara, A. R. Measurement of Aerosol Optical Extinction at with Pulsed Cavity Ring down Spectroscopy. *J. Aerosol Sci.* **2004**, *35*, 995–1011.
- (8) Miles, R. E. H.; Rudić, S.; Orr-Ewing, A. J.; Reid, J. P. Sources of Error and Uncertainty in the Use of Cavity Ring Down Spectroscopy to Measure Aerosol Optical Properties. *Aerosol Sci. Technol.* **2011**, *45*, 1360–1375.
- (9) Mason, B. J.; King, S.-J.; Miles, R. E. H.; Manfred, K. M.; Rickards, A. M. J.; Kim, J.; Reid, J. P.; Orr-Ewing, A. J. Comparison of the Accuracy of Aerosol Refractive Index Measurements from Single Particle and Ensemble Techniques. *J. Phys. Chem. A* **2012**, *116*, 8547–8556.
- (10) Lang-Yona, N.; Rudich, Y.; Segre, E.; Dinar, E.; Abo-Riziq, A. Complex Refractive Indices of Aerosols Retrieved by Continuous Wave-Cavity Ring down Aerosol Spectrometer. *Anal. Chem.* **2009**, *81*, 1762–1769.
- (11) Riziq, A. A.; Trainic, M.; Erlick, C.; Segre, E.; Rudich, Y. Extinction Efficiencies of Coated Absorbing Aerosols Measured by Cavity Ring down Aerosol Spectrometry. *Atmos. Chem. Phys. Discuss.* **2007**, *7*, 18113–18144.
- (12) Miles, R. E. H.; Rudić, S.; Orr-Ewing, A. J.; Reid, J. P. Measurements of the Wavelength Dependent Extinction of Aerosols by Cavity Ring down Spectroscopy. *Phys. Chem. Chem. Phys.* **2010**, *12*, 3914–3920.
- (13) Michel Flores, J.; Bar-Or, R. Z.; Bluvshtein, N.; Abo-Riziq, A.; Kostinski, A.; Borrman, S.; Koren, I.; Rudich, Y. Absorbing Aerosols at High Relative Humidity: Linking Hygroscopic Growth to Optical Properties. *Atmos. Chem. Phys.* **2012**, *12*, 5511–5521.
- (14) Freedman, M. A.; Hasenkopf, C. A.; Beaver, M. R.; Tolbert, M. A. Optical Properties of Internally Mixed Aerosol Particles Composed of Dicarboxylic Acids and Ammonium Sulfate. *J. Phys. Chem. A* **2009**, *113*, 13584–13592.
- (15) Miller, J. L.; Orr-Ewing, A. J. Cavity Ring-down Spectroscopy Measurement of Single Aerosol Particle Extinction. II. Extinction of Light by an Aerosol Particle in an Optical Cavity Excited by a CW Laser. *J. Chem. Phys.* **2007**, *126*, 174303.
- (16) Butler, T. J. A.; Miller, J. L.; Orr-Ewing, A. J. Cavity Ring-down Spectroscopy Measurements of Single Aerosol Particle Extinction. I. The Effect of Position of a Particle within the Laser Beam on Extinction. *J. Chem. Phys.* **2007**, *126*, 174302.
- (17) Walker, J. S.; Carruthers, A. E.; Orr-Ewing, A. J.; Reid, J. P. Measurements of Light Extinction by Single Aerosol Particles. *J. Phys. Chem. Lett.* **2013**, *4*, 1748–1752.
- (18) McGloin, D.; Dholakia, K. Bessel Beams: Diffraction in a New Light. *Contemp. Phys.* **2005**, *46*, 15–28.
- (19) Cotterell, M. I.; Mason, B. J.; Carruthers, A. E.; Walker, J. S.; Orr-Ewing, A. J.; Reid, J. P. Measurements of the Evaporation and Hygroscopic Response of Single Fine-Mode Aerosol Particles Using a Bessel Beam Optical Trap. *Phys. Chem. Chem. Phys.* **2014**, *16*, 2118–2128.
- (20) Mason, B. J.; Walker, J. S.; Reid, J. P.; Orr-Ewing, A. J. Deviations from Plane-Wave Mie Scattering and Precise Retrieval of Refractive Index for a Single Spherical Particle in an Optical Cavity. *J. Phys. Chem. A* **2014**, *118*, 2083–2088.
- (21) Tang, I.; Munkelwitz, H. Water Activities, Densities, and Refractive Indices of Aqueous Sulfates and Sodium Nitrate Droplets of Atmospheric Importance. *J. Geophys. Res.* **1994**, *99*, 18801–18800.
- (22) Tang, I. N.; Tridico, A. C.; Fung, K. H. Thermodynamic and Optical Properties of Sea Salt Aerosols. *J. Geophys. Res.* **1997**, *102*, 23269–23275.
- (23) Tang, I.; Munkelwitz, H. Simultaneous Determination of Refractive Index and Density of an Evaporating Aqueous Solution Droplet. *Aerosol Sci. Technol.* **1991**, *15*, 37–41.
- (24) Tang, I. Chemical and Size Effects of Hygroscopic Aerosols on Light Scattering Coefficients. *J. Geophys. Res.* **1996**, *101*, 19245–19250.
- (25) Textor, C.; Schulz, M.; Guibert, S.; Kinne, S.; Balkanski, Y.; Bauer, S.; Berntsen, T.; Berglen, T.; Boucher, O.; Chin, M.; et al. Analysis and Quantification of the Diversities of Aerosol Life Cycles within AeroCom. *Atmos. Chem. Phys.* **2006**, *6*, 1777–1813.

- (26) Johnson, G. R.; Ristovski, Z.; Morawska, L. Method for Measuring the Hygroscopic Behaviour of Lower Volatility Fractions in an Internally Mixed Aerosol. *J. Aerosol Sci.* **2004**, *35*, 443–455.
- (27) Dinar, E.; Abo Riziq, A.; Spindler, C.; Erlick, C.; Kiss, G.; Rudich, Y. The Complex Refractive Index of Atmospheric and Model Humic-like Substances (HULIS) Retrieved by a Cavity Ring down Aerosol Spectrometer (CRD-AS). *Faraday Discuss.* **2008**, *137*, 279–295.
- (28) Walker, J. S.; Wills, J. B.; Reid, J. P.; Wang, L.; Topping, D. O.; Butler, J. R.; Zhang, Y.-H. Direct Comparison of the Hygroscopic Properties of Ammonium Sulfate and Sodium Chloride Aerosol at Relative Humidities Approaching Saturation. *J. Phys. Chem. A* **2010**, *114*, 12682–12691.
- (29) Preston, T. C.; Mason, B. J.; Reid, J. P.; Luckhaus, D.; Signorell, R. Size-Dependent Position of a Single Aerosol Droplet in a Bessel Beam Trap. *J. Opt.* **2014**, *16*, 025702.
- (30) Zuend, A.; Marcolli, C.; Booth, A. M.; Lienhard, D. M.; Soonsin, V.; Krieger, U. K.; Topping, D. O.; McFiggans, G.; Peter, T.; Seinfeld, J. H. New and Extended Parameterization of the Thermodynamic Model AIOMFAC: Calculation of Activity Coefficients for Organic-Inorganic Mixtures Containing Carboxyl, Hydroxyl, Carbonyl, Ether, Ester, Alkenyl, Alkyl, and Aromatic Functional Groups. *Atmos. Chem. Phys.* **2011**, *11*, 9155–9206.
- (31) Rheims, J.; Köser, J.; Wriedt, T. Refractive-Index Measurements in the near-IR Using an Abbe Refractometer. *Meas. Sci. Technol.* **1997**, *8*, 801.
- (32) Tang, I.; Munkelwitz, H. Composition and Temperature Dependence of the Deliquescence Properties of Hygroscopic Aerosols. *Atmos. Environ., Part A* **1993**, *27A*, 467–473.
- (33) Millard, R.; Seaver, G. An Index of Refraction Algorithm for Seawater over Temperature, Pressure, Salinity, Density, and Wavelength. *Deep-Sea Res., Part A* **1990**, *37*, 1909–1926.
- (34) Gao, Y.; Chen, S. B.; Yu, L. E. Efflorescence Relative Humidity of Airborne Sodium Chloride Particles: A Theoretical Investigation. *Atmos. Environ.* **2007**, *41*, 2019–2023.
- (35) Wise, M. E.; Biskos, G.; Martin, S. T.; Russell, L. M.; Buseck, P. R. Phase Transitions of Single Salt Particles Studied Using a Transmission Electron Microscope with an Environmental Cell. *Aerosol Sci. Technol.* **2005**, *39*, 849–856.